Two-body loss rates for reactive collisions of cold atoms

C. Cop[*] and R. Walser

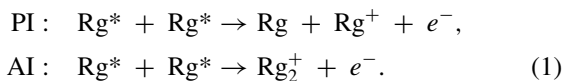*TU Darmstadt, Institut für Angewandte Physik, D-64289 Darmstadt, Germany*

We present an effective two-channel model for reactive collisions of cold atoms. It augments elastic molecular channels with an irreversible, inelastic loss channel. Scattering is studied with the distorted-wave Born approximation and yields general expressions for angular momentum resolved cross sections as well as two-body loss rates. Explicit expressions are obtained for piecewise constant potentials. A pole expansion reveals simple universal shape functions for cross sections and two-body loss rates in agreement with the Wigner threshold laws. This is applied to collisions of metastable ^{20}Ne and ^{21}Ne atoms, which decay primarily through exothermic Penning or associative ionization processes. From a numerical solution of the multichannel Schrödinger equation using the best currently available molecular potentials, we have obtained synthetic scattering data. Using the two-body loss shape functions derived in this paper, we can match these scattering data very well.

I. INTRODUCTION

Understanding reactive collisions of metastable rare gas atoms (Rg*) is a central topic in trapping such species. Major loss processes in Rg* collisions are Penning ionization (PI) and associative ionization (AI) [1,2]

$$\text{PI}: \quad \text{Rg*} + \text{Rg*} \rightarrow \text{Rg} + \text{Rg}^+ + e^-,$$
$$\text{AI}: \quad \text{Rg*} + \text{Rg*} \rightarrow \text{Rg}_2^+ + e^-. \tag{1}$$

In current trapping experiments [3], it is possible to observe the reaction kinetic with high resolution and in real time, as the ionic fragments can be detected with single-ion precision.

In order to parametrize cold ionizing collisions such as PI and AI, different models have been presented. The quantum reflection model [4] has been applied successfully to explain two-body loss rates in cold collisions of metastable rare gas atoms, for He* collisions [5–7], Xe* collisions [8], and Kr* collisions [9]. This model assumes complete ionization at short range and predicts universal scattering rates for collisions of different isotope mixtures in agreement with mass scaling.

Current cold Ne* experiments of Birkl *et al.* [10–12] have provided new data on elastic as well as inelastic scattering. The isotope composition of the Ne gas consists of the bosonic (B) and fermionic (F) isotopes with natural abundance, i.e., ^{20}Ne (90.48%, B), ^{21}Ne (0.27%, F), ^{22}Ne (9.25%, B) [13]. Homonuclear [10,12] and heteronuclear collision rates [11] were obtained, preparing polarized as well as unpolarized subensembles with respect to the internal magnetic substates. The experiment uncovers deviations from a fundamental mass scaling law for the elastic and inelastic scattering rates of different isotopes. Thus, a simple quantum reflection model is insufficient.

To match these experimental facts, we consider an effective two-channel model using molecular potentials [14,15] with van der Waals interaction at long range [16] for the elastic channels

as shown in Fig. 1. The free parameters of the fictitious inelastic loss potential, as well as the coupling strength, were obtained from a finite-temperature fit to the scattering data with very good agreement. The threshold scattering rates of the numerical two-channel model are also in very good agreement with recent nonuniversal models for reactive collisions [17–19], which have been applied successfully to atom-ion collisions [20], polar molecule collisions [21–25], and collisions of other species [26]. For details, we refer to Ref. [27].

In this article, we will complement the numerical approach with an analytical study of the two-channel model using piecewise constant couplings and potentials only. Within this hypothesis, scattering can be studied analytically in the complex k or E plane. The coupling strength between the molecular channel and the loss channel should be weak on physical grounds. Therefore, we will employ the distorted-wave Born approximation (DWBA), which is introduced in Sec. II and yields a general expression for the partial-wave resolved two-body loss rates. Moreover, we introduce the concepts of the pole expansion of the S matrix. Coupled square wells are an illuminating application of the previous discussion. Exact and DBWA solutions are presented in Sec. III. However, even this simple model yields explicit expressions, which are too complex for interpretation. Therefore, we will step back to single-channel scattering in Sec. IV and revisit the well-known results s-, p-, and d-wave scattering phases and cross sections [28]. Already there, the complex analytical expression conceals the essential physics, which is uncovered only by a pole expansion. In Sec. V, we merge the insights from the previous sections and study the two-body loss rates. Exact square-well results for s, p, and d waves are compared to explicit expressions (shape functions) using the pole approximation. These shape functions are consistent with the Wigner threshold laws and are depicted for some suitably chosen parameters. Finally, in Sec. VI, we demonstrate the utility of these physically motivated shape functions. While originally derived for square-well potentials, they are also very well suited to interpolate synthetic scattering data obtained from the two-channel van
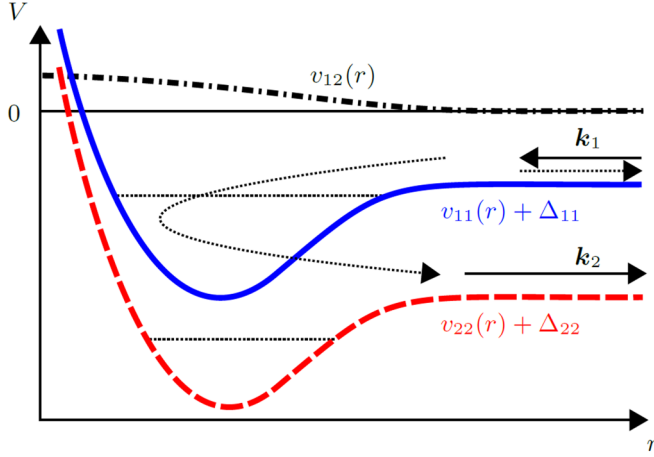
---

*christiancop@online.de

FIG. 1. Effective two-channel reaction model: molecular scattering channel 1 coupled to loss channel 2. Radial molecular potentials $v_{11}(r)$ (solid, blue line) and loss potential $v_{22}(r)$ (dashed, red line) are coupled by $v_{12}(r)$ (dashed-dotted, black line). At large separations, the potentials approach the channel thresholds Δ_{ii} with $\Delta_{11} > \Delta_{22}$ and all couplings $v_{ij}(r)$ vanish. The straight thin dashed black lines indicate bound states.

der Waals model for the ^{20}Ne and ^{21}Ne collisions [27]. The article ends with conclusions and two appendices regarding definitions of Riccati-Bessel functions and details on the pole expansion in the complex plane.

II. MULTICHANNEL SCATTERING

In order to understand the reactive quantum kinetics of Eqs. (1) quantitatively, one needs to consider two coupled channels, as depicted in Fig. 1. There, a molecular state manifold or channel 1 can either scatter elastically within the manifold, or inelastically to a loss channel 2. This removes particles irreversibly from the interaction zone. In the rest frame of the collision partners, the state manifold $\mathscr{H} = \mathrm{span}\{\boldsymbol{k} \in \mathbb{R}^3, i \in \{1,2\} | |\boldsymbol{k},i\rangle\}$ is spanned by plane waves decorated with a channel subscript. The energy

$$H = H_0 + V(r) \qquad (2)$$

consists of an asymptotically free Hamiltonian operator H_0 and a short-range, matrix-valued potential $V(r)$. To keep the notation compact, we will use natural units $\hbar = 2\mu = 1$, with the reduced mass of the collision partners $\mu = m_1 m_2/(m_1 + m_2)$. Thus, $H_0 = \boldsymbol{p}^2 + \Delta$ denotes the relative kinetic energy of the collision partners with respect to the collision threshold energies $\Delta_{ij} = \delta_{ij}\Delta_{ii}$ with $\Delta_{11} > \Delta_{22}$. Plane waves are eigenfunctions of the noninteracting two-particle system

$$H_0|\boldsymbol{k},i\rangle = E|\boldsymbol{k},i\rangle, \quad E = k_i^2 + \Delta_{ii}, \qquad (3)$$

with channel wave numbers $k_i(E) = \sqrt{E - \Delta_{ii}}$ determined by the energy E relative to the threshold energies Δ_{ii}. The short-range molecular potential

$$V = V^{\mathrm{I}} + V^{\mathrm{II}} = \begin{pmatrix} v_{11} & 0 \\ 0 & v_{22} \end{pmatrix} + \begin{pmatrix} 0 & v_{12} \\ v_{12}^* & 0 \end{pmatrix} \qquad (4)$$

can be decomposed into the potentials V^{I} for each individual channel and their coupling V^{II}.

A. Two-potential formula for the T matrix

Scattering in the presence of two potentials can be described using the two-potential formula [29] for the T-matrix elements

$$\begin{aligned} t_{ij}(\boldsymbol{k}_i,\boldsymbol{k}_j) &= \langle \boldsymbol{k}_i,i|T|\boldsymbol{k}_j,j\rangle \\ &= \langle \boldsymbol{k}_i,i|V^{\mathrm{I}}|\boldsymbol{k}_j,j,+^{\mathrm{I}}\rangle + \langle \boldsymbol{k}_i,i,-^{\mathrm{I}}|V^{\mathrm{II}}|\boldsymbol{k}_j,j,+\rangle. \end{aligned} \qquad (5)$$

This expression introduces the scattering states $|\boldsymbol{k}_i,i,\pm^{\mathrm{I}}\rangle$ that are obtained in the absence of potential V^{II} and the fully coupled scattering states $|\boldsymbol{k}_i,i,\pm\rangle$. They are defined by their corresponding Lippmann-Schwinger equations as

$$|\boldsymbol{k}_i,i,\pm^{\mathrm{I}}\rangle = |\boldsymbol{k}_i,i\rangle + G_0^\pm(E)_{ii} v_{ii}^{\mathrm{I}} |\boldsymbol{k}_i,i,\pm^{\mathrm{I}}\rangle, \qquad (6)$$

$$|\boldsymbol{k}_i,i,\pm\rangle = |\boldsymbol{k}_i,i\rangle + \sum_{j=1}^{2} G_0^\pm(E)_{ii} v_{ij} |\boldsymbol{k}_j,j,\pm\rangle, \qquad (7)$$

with $G_0^\pm(E) \equiv \lim_{\epsilon\to+0}(E \pm i\epsilon - H_0)^{-1}$ denoting the free advanced $(-)$ and retarded $(+)$ Green's functions.

The exact result (5) is most useful if the second potential is weak and the Born series expansion is applicable. To first order, the distorted-wave Born approximation for the T matrix reads as

$$\begin{aligned} t_{ij}(\boldsymbol{k}_i,\boldsymbol{k}_j) &= t_{ij}^{(0)}(\boldsymbol{k}_i,\boldsymbol{k}_j) + t_{ij}^{(1)}(\boldsymbol{k}_i,\boldsymbol{k}_j) + O(V^{\mathrm{II}2}) \\ &= \langle \boldsymbol{k}_i,i|V^{\mathrm{I}}|\boldsymbol{k}_j,j,+^{\mathrm{I}}\rangle + \langle \boldsymbol{k}_i,i,-^{\mathrm{I}}|V^{\mathrm{II}}|\boldsymbol{k}_j,j,+^{\mathrm{I}}\rangle \\ &\quad + \cdots. \end{aligned} \qquad (8)$$

It is important to note that first-order corrections due to the second potential only occur in the off-diagonal $t_{i\neq j}$ matrix element.

B. Scattering states in terms of Jost functions

To proceed in the analysis of reactive two-body scattering, we will assume rotational invariant interactions [27]. This implies angular momentum conservation and suggests to use symmetry-adapted, spherical coordinates (r,θ,ϕ). Single-channel scattering states with outgoing or incoming asymptotics $(\pm)$ are conventionally [29] defined as

$$\langle \mathbf{x}|E,l,m,\pm\rangle = i^l \left(\frac{2}{\pi\sqrt{E}}\right)^{1/2} \frac{\psi_l^\pm(E,r)}{r} Y_{lm}(\theta,\phi), \qquad (9)$$

with the reduced scalar wave functions $\psi_l^\pm(E,r)$, the eigenvalues of the angular projection m on the quantization axis z and angular momentum l. If this is generalized to multichannel scattering, the Schrödinger equation (2) reads as

$$\left[K^2(E) + \partial_r^2 - V(r) - \frac{l(l+1)}{r^2}\right]\Psi_l^\pm(E,r) = 0, \qquad (10)$$

where the wave-number matrix $K_{ij}(E) = \delta_{ij}k_i(E)$ is defined by the individual channel wave numbers $k_i(E)$ as in Eq. (3). In turn, the reduced scattering wave function

$$\Psi_l^\pm(E,r) = \begin{pmatrix} \psi_{l,11}^\pm(E,r) & \psi_{l,12}^\pm(E,r) \\ \psi_{l,21}^\pm(E,r) & \psi_{l,22}^\pm(E,r) \end{pmatrix} \qquad (11)$$

becomes a 2×2 matrix to account for the two linearly independent solutions in the scattering channels. They are determined

from the boundary condition at the origin

$$\Psi_l^{\pm}(E, r = 0) = 0 \tag{12}$$

and the asymptotic behavior for the outgoing solution

$$\Psi_l^+(E, r) \xrightarrow[r \to \infty]{} \frac{i}{2} \left\{ \hat{h}_l^-(Kr) - \frac{\hat{h}_l^+(Kr)}{\sqrt{K}} S_l(E) \sqrt{K} \right\}, \tag{13}$$

as well as $\Psi_l^- = (\Psi_l^+)^\dagger$. Here, $\hat{h}_l^\pm$ are the Riccati-Hankel functions as defined in Appendix A and $S_l(E)$ denotes the S matrix with angular momentum l.

The *regular solution* $\Phi_l(E, r)$ is another solution to the Schrödinger equation (10). It is defined by the boundary condition at the origin

$$\Phi_l(E, r) \xrightarrow[r \to 0]{} \hat{j}_l(Kr). \tag{14}$$

In each channel, the solution approaches a Riccati-Bessel function $\hat{j}_l(k_i r)$ close to the origin and is smaller in amplitude in all other coupled channels (cf. Appendix A). Since the coupled radial Schrödinger equation (10) and the boundary condition (14) are real for real energies, the regular solution is real as well. In the asymptotic region, the regular solution reads as

$$\Phi_l(E, r) \xrightarrow[r \to \infty]{} \frac{i}{2} \{ \hat{h}_l^-(Kr) \mathscr{F}_l(K) - \hat{h}_l^+(Kr) \mathscr{F}_l(-K) \}, \tag{15}$$

with the Jost matrix $\mathscr{F}_l(K)$ and its matrix elements $\mathscr{f}_{l,ij}$. Comparing the asymptotic form of the scattering wave function (13) to the asymptotic form of the regular solution (15) leads to the relation of the scattering wave function and the regular solution, given by

$$\psi_l^+(E, r) = \Phi_l(E, r) \mathscr{F}_l^{-1}(K), \tag{16}$$

and to the relation of the Jost matrix and the S matrix

$$S_l(E) = \sqrt{K} \mathscr{F}_l(-K) \mathscr{F}_l^{-1} / \sqrt{K}. \tag{17}$$

Using the constitutive relation between the S and the T operator

$$S(E) = \mathbb{1} - 2\pi i \delta(E - H_0) T(E), \tag{18}$$

one can connect all relevant entities. Within the distorted-wave Born approximation from Eq. (8), the S matrix reads as to first order

$$S_l(E) = \begin{pmatrix} s_{l,11}^{(0)}(E) & s_{l,12}^{(1)}(E) \\ s_{l,21}^{(1)}(E) & s_{l,22}^{(0)}(E) \end{pmatrix} + O(V^{\text{II}^2}), \tag{19}$$

where the diagonal S-matrix elements

$$s_{l,ii}^{(0)}(E) = \frac{\mathscr{f}_{l,ii}^{(0)}(-k_i(E))}{\mathscr{f}_{l,ii}^{(0)}(k_i(E))} = e^{2i\eta_{l,i}(k_i(E))} \tag{20}$$

are the uncoupled solutions for the potential V_{I} and given in terms of the uncoupled Jost functions $\mathscr{f}_{l,ii}^{(0)}(k_i)$ or equivalently by scattering phases $\eta_{l,i}(k_i)$. For the sake of readability, we have not included a further superscript (0) in the scattering phase. The scattering phases

$$\eta_{l,i}(k_i(E)) = \eta_{l,i}^b(k_i(E)) + \eta_{l,i}^r(k_i(E)) \tag{21}$$

can be decomposed into a background contribution $\eta_{l,i}^b$, which is a slowly varying function of k_i and a resonant contribution

$\eta_{l,i}^r$, which changes rapidly across a resonance. With this decomposition we can write for the S-matrix elements

$$s_{l,ii}^{(0)}(E) = s_{l,ii}^{(0)b}(E) s_{l,ii}^{(0)r}(E). \tag{22}$$

In the following, we prefer to switch from the energy parameter E to the wave number k. All functions will become functions of $k_i(E)$ while being implicitly functions of E due to Eq. (3). The observable available for measurement is the partial elastic scattering cross section [29]

$$\sigma_{l,ii}^{(0)}(k_i) = 2\pi \frac{2l+1}{k_i^2} \left[1 - \Re s_{l,ii}^{(0)}(k_i) \right]. \tag{23}$$

The cross section for scattering of channel 1 to channel 2 in the DWBA is given by

$$\sigma_{l,12}^{(1)}(k_1) = \pi \frac{2l+1}{k_1^2} \left| s_{l,12}^{(1)}(k_1) \right|^2. \tag{24}$$

The off-diagonal S-matrix elements are obtained from the DWBA approximation (8) and the constitutive relation (18) as

$$s_{l,12}^{(1)}(E) = \frac{2 \int_0^\infty dr \, \psi_{l,11}^{(0)+}(E, r) v_{12}^{\text{II}}(r) \psi_{l,22}^{(0)+}(E, r)}{i \sqrt{k_1 k_2}}$$
$$= e^{2i\eta_{l,12}(k_1(E))}, \tag{25}$$

where $\psi_{l,ii}^{(0)+}(E, r)$ are the uncoupled solutions of the radial Schrödinger equation (10) for the potential V^{I} only, using $(\psi_{l,ii}^{(0)-}(E))^* = \psi_{l,ii}^{(0)+}(E)$. The complex phase $\eta_{l,12}(k_1) \in \mathbb{C}$ considers also attenuation and can be decomposed into a resonance and a background contribution as in Eq. (21).

The observable for measurement of atom loss in channel 1 is the two-body loss rate [8] which is given in terms of the cross section from channel 1 to channel 2:

$$\beta_l^{(1)}(k_1) = 2k_1 \sigma_{l,12}^{(1)}(k_1) = 2\pi \frac{2l+1}{k_1} |s_{l,12}^{(1)}(k_1)|^2. \tag{26}$$

It quantifies the loss of probability current from the elastic scattering channel 1.

C. Pole expansion of the S matrix

Scattering theory greatly benefits from complex analysis and the continuation of real parameters, like the energy E or the wave number k, into the complex plane. For finite-range potentials, it can be shown that the Jost functions are entire functions of k. Then, the S matrix is analytic everywhere in the complex E or k plane except at singular points, when the Jost function vanishes [29].

For complex channel wave numbers k_i, the analytic continuation of the uncoupled Jost functions reads as

$$\mathscr{f}_l(k)^* = \mathscr{f}_l(-k^*). \tag{27}$$

With the help of the Weierstrass factorization theorem [30–32], one can express the Jost function

$$\mathscr{f}_l(k) = \mathscr{f}_l(0) e^{ik} \prod_{n=1}^{N'} \left(1 - i \frac{k}{\varkappa_n} \right) \prod_{n=1}^{N} \left(1 + i \frac{k}{\mathscr{K}_n} \right)$$
$$\times \prod_{n=1}^{\infty} \left(1 + \frac{k}{\mathscr{k}_n^*} \right) \left(1 - \frac{k}{\mathscr{k}_n} \right) \tag{28}$$
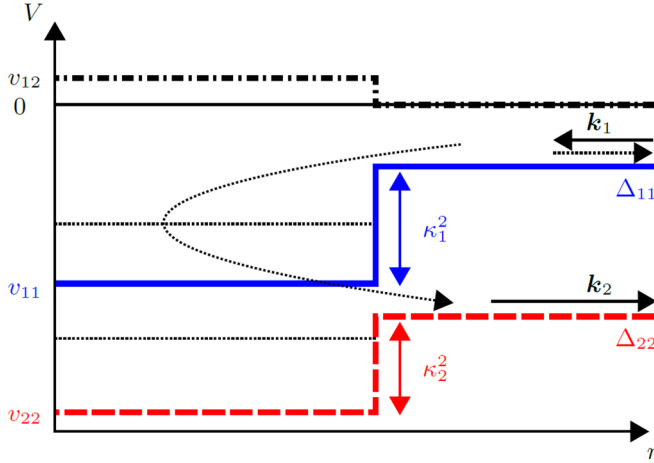
FIG. 2. Effective two-channel square-well potential vs radius r. Within the range $r < 1$, the potentials v_{11} (solid, blue line), v_{22} (dashed, red line), and v_{12} (dashed-dotted, black line) are constant. For radii $r > 1$, the potential matrix decouples into the channel thresholds Δ_{11} and Δ_{22}. The channel wave numbers k_1, k_2 are defined as in Eq. (3). The straight thin dashed black lines indicate bound states.

as an infinite product of its zeros. For each of the N' virtual states of the scattering potential, there is a zero of the Jost function on the negative imaginary axis at $k = -i\varkappa_n$ with $\varkappa_n > 0$. For each of the N bound states, the Jost function vanishes on the positive imaginary axis at $k = i\mathscr{K}_n$ with $\mathscr{K}_n > 0$. Moreover, there are always infinitely many scattering resonances of the potential, which correspond to the zeros of the Jost function at $k = \mathscr{k}_n$ and $k = -\mathscr{k}_n^*$ with $\Re \mathscr{k}_n > 0$.

From this representation of the Jost function, one obtains the S matrix of Eq. (20) as an infinite product of poles in the complex $k = k(E)$ plane

$$
s_l(E) = e^{-2ik} \prod_{n=1}^{N'} \frac{\varkappa_n + ik}{\varkappa_n - ik} \prod_{n=1}^{N} \frac{\mathscr{K}_n - ik}{\mathscr{K}_n + ik} \prod_{n=1}^{\infty} \frac{\mathscr{k}_n + k}{\mathscr{k}_n - k} \frac{\mathscr{k}_n^* - k}{\mathscr{k}_n^* + k}
$$

$$
= e^{2i\eta_l^b(k)} s_l^r(E). \tag{29}
$$

For low-energy collisions, the analytical behavior of the S matrix is dominated by the resonant contribution s_l^r originating from states closest to the energy threshold. The effect of the infinitely many other poles of the pole expansion can be summarized in a slowly varying background scattering phase η_l^b.

III. COUPLED SQUARE WELLS

In order to put these general considerations to practical use, we will study an elementary example of a weakly coupled square-well potential, which is shown in Fig. 2. There, the piecewise constant potential matrix reads as

$$
v_{ij}(r) = \begin{cases} v_{ij}, & r \leqslant 1 \\ \Delta_{ij}, & r > 1. \end{cases} \tag{30}
$$

The two levels $i \in \{1,2\}$ are coupled within a radius $r < 1$ and decouple outside $\Delta_{i \neq j} = 0$. The depths of the attractive potentials are parametrized by κ_i and the inner level spacing is

conveniently abbreviated by δv as

$$
\kappa_i^2 = \Delta_{ii} - v_{ii} > 0, \tag{31a}
$$

$$
\delta v = v_{11} - v_{22}. \tag{31b}
$$

The utility of the model is seen by solving it perturbatively in Sec. III A and exactly in Sec. III B. The complexity of the solution conceals resonances and a simple interpretation is possible only by the pole expansion presented in Sec. IV, eventually.

A. Distorted-wave Born approximation

First, to initialize the DWBA, we need the solution for the uncoupled square-well Schrödinger equation (10) with $v_{12} = 0$. In the inner and outer regions, the solution reads as

$$
\psi_{l,ii}^{(0)+}(E,r) = \begin{cases} \left(\frac{k_i}{q_i}\right)^{l+1} \frac{\hat{j}_l(q_i r)}{\mathscr{f}_{l,ii}^{(0)}(k_i)}, & r \leqslant 1 \\ \frac{s_{l,ii}^{(0)}(E)\hat{h}_l^+(k_i r) - \hat{h}_l^-(k_i r)}{2i}, & r > 1 \end{cases} \tag{32}
$$

where we have introduced channel wave numbers q_i and k_i for the inner and outer regions

$$
q_1^2 \equiv E - v_{11} = k_1^2 + \kappa_1^2, \tag{33}
$$

$$
q_2^2 \equiv E - v_{22} = k_2^2 + \kappa_2^2, \tag{34}
$$

and k_i as in Eq. (3). The ansatz for the wave function of Eq. (32) introduces the Jost function $\mathscr{f}_{l,ii}^{(0)}(k_i)$ by the relation between the regular solution at the origin (14) and the scattering solution (16). By matching the wave function smoothly at $r = 1$, one obtains the Jost function $\mathscr{f}_{l,ii}^{(0)}(k_i) = g_l(k_i, q_i(k_i))$, from the auxiliary function

$$
g_l(k,q) = 2i\left[\frac{k}{q}\right]^l \frac{q \hat{j}_l'(q)\hat{h}_l^+(k) - k \hat{h}_l^{+'}(k)\hat{j}_l(q)}{q[\hat{h}_l^{+'}(k)\hat{h}_l^-(k) - \hat{h}_l^{-'}(k)\hat{h}_l^+(k)]}, \tag{35}
$$

and the S-matrix elements from Eq. (20) as

$$
s_{l,ii}^{(0)}(E) = \frac{q_i \hat{j}_l'(q_i)\hat{h}_l^-(k_i) - k_i \hat{h}_l^{-'}(k_i)\hat{j}_l(q_i)}{q_i \hat{j}_l'(q_i)\hat{h}_l^+(k_i) - k_i \hat{h}_l^{+'}(k_i)\hat{j}_l(q_i)}. \tag{36}
$$

Second, in the next order of the DWBA the transition matrix element reads as

$$
s_{l,12}^{(1)}(E) = \frac{2v_{12}}{i\delta v\sqrt{k_1 k_2}}\left(\frac{k_1 k_2}{q_1 q_2}\right)^{l+1} \frac{1}{\mathscr{f}_{l,11}^{(0)}(k_1)\mathscr{f}_{l,22}^{(0)}(k_2)}
$$

$$
\times [q_1 \hat{j}_{l-1}(q_1)\hat{j}_l(q_2) - q_2 \hat{j}_{l-1}(q_2)\hat{j}_l(q_1)], \tag{37}
$$

using Eqs. (25) and (32). Thus, we obtain the interesting result that the transition matrix elements are given in terms of the uncoupled Jost functions. Thus, their zeros determine the poles of the S-matrix elements.

B. Exact solution

Obtaining the full Jost matrix $\mathscr{f}_l$ for the coupled square well analytically is a standard exercise. By matching the wave function at the intersection, one finds for the diagonal

elements

$$\mathcal{f}_{l,11}(k_1) = g_l(k_1, q_+) \cos^2 \alpha + g_l(k_1, q_-) \sin^2 \alpha, \qquad (38)$$

$$\mathcal{f}_{l,22}(k_2) = g_l(k_2, q_-) \cos^2 \alpha + g_l(k_2, q_+) \sin^2 \alpha, \qquad (39)$$

and for the off-diagonal elements

$$\mathcal{f}_{l,12}(k_1) = \frac{\sin 2\alpha}{2} \left[\frac{k_2}{k_1} \right]^{l+1} [g_l(k_1, q_+) - g_l(k_1, q_-)], \qquad (40)$$

$$\mathcal{f}_{l,21}(k_2) = \frac{\sin 2\alpha}{2} \left[\frac{k_1}{k_2} \right]^{l+1} [g_l(k_2, q_+) - g_l(k_2, q_-)], \qquad (41)$$

defining a mixing angle α by $\tan 2\alpha = 2v_{12}/\delta v$. The linearly independent solutions of the Schrödinger equation in the inner region are characterized by the two wave numbers $q_\pm = \sqrt{k^2 - \varepsilon_\pm}$, with an energy splitting

$$\varepsilon_\pm = \tfrac{1}{2}\left(v_{11} + v_{22} \pm \sqrt{\delta v^2 + 4v_{12}^2} \right). \qquad (42)$$

Finally, the solution for the S matrix can be found from the Jost matrix by Eq. (17). In particular, we are interested in the off-diagonal element and find

$$s_{l,12}(E) = \sqrt{\frac{k_1}{k_2}} \frac{\mathcal{f}_{l,12}^*(k_1)\mathcal{f}_{l,11}(k_1) - \mathcal{f}_{l,11}^*(k_1)\mathcal{f}_{l,12}(k_1)}{\mathcal{f}_{l,11}(k_1)\mathcal{f}_{l,22}(k_2) - \mathcal{f}_{l,12}(k_1)\mathcal{f}_{l,21}(k_2)}, \qquad (43)$$

with $k_i \equiv k_i(E)$. Clearly, one recovers the DWBA expression for $s_{l,12}^{(1)}$ of Eq. (37) from a first-order expansion in $O(v_{12}/\delta v)$.

IV. SINGLE-CHANNEL SCATTERING

The understanding of the coupled-channel scattering process is complex as single-channel scattering resonances are intertwined with two-channel mixing. It is therefore prudent to dissect the problem and analyze single-channel scattering first. This is achieved by turning off the coupling $v_{12} = 0$ between the channels and to study scattering in channel 1 exclusively. Now, we have the freedom to set the threshold energy $\Delta_{11} = 0$.

With the goal of parametrizing cross sections and loss rates for cold collisions of atoms analytically, we only consider the lowest s, p, d partial waves. We will not exhaustively study all conceivable cases, but demonstrate the benefits of the pole expansion for certain instances. In particular, for s waves, we consider a potential with a single weakly bound state in Sec. IV A and in Sec. IV B for p and d waves with a single quasibound state. These states dominate the behavior of the cross sections. We will compare exact square-well results to the results from a single-pole expansion due to the weakly bound state for s waves and from a two-pole expansion due to the quasibound states for p and d waves, eventually.

To enhance the visibility of resonances in the examples, we have deliberately chosen different potential depths for each angular momentum channel as listed in Table I.

A. Scattering in the s channel

Shallow three-dimensional attractive square wells can have zero, one, or more bound states. By increasing the potential depth continuously, a virtual state with positive energy transforms into a half bound state at zero energy and becomes a

TABLE I. Potential depth κ_1^2, complex zero k_1 of Jost function $\mathcal{f}_{l,11}^{(0)}(k_1)$, and binding or resonance energy $E_r = \Re^2 k_1 - \Im^2 k_1$ in the uncoupled channel 1 for different angular momenta. Potential depths were deliberately chosen individually, so that each potential only supports one bound state (s) or one quasibound state (p,d).

Angular momentum	l	$0\,(s)$	$1\,(p)$	$2\,(d)$
Potential depth	κ_1^2	4.0	9.0	19.5
Zero of Jost function	k_1	$0.638i$	0.539	0.628
			$-0.100i$	$-0.009i$
Binding/resonance energy	E_r	-0.407	0.281	0.395

bound state with negative energy, eventually. In the following, we will present the exact scattering phase and cross section for s waves and compare these with the pole expansion approximations.

1. Exact solution

For $l = 0$, the Jost function of Eq. (35) reads as

$$\mathcal{f}_{0,11}^{(0)}(k_1) = \frac{e^{ik_1} \sin q_1}{q_1}(q_1 \cot q_1 - ik_1), \qquad (44)$$

and the S-matrix element follows from Eq. (20) as

$$s_{0,11}^{(0)}(k_1) = e^{-2ik_1} \frac{q_1 \cot q_1 + ik_1}{q_1 \cot q_1 - ik_1}. \qquad (45)$$

For real k_1, it is unimodular $|s_{0,11}^{(0)}| = 1$ and the real scattering phase reads as

$$\eta_0(k_1) = n\pi - k_1 + \arctan \frac{k_1}{q_1 \cot q_1}, \qquad (46)$$

where Levinson theorem [29] determines the zero-energy phase from the number of bound states n in the scattering potential.

2. Single-pole expansion

To be specific, we will consider the s-potential with well depth κ_1^2 given in Table I, which only supports one weakly bound state. It emerges as a zero of the Jost function $f_{0,11}^{(0)}(k_1) = 0$ at $k_1 = i\mathcal{K}_1$ in the complex k_1 plane. Its zero contours are shown in Fig. 3. For wave numbers close to threshold, we assume that the Weierstrass expansion (28) is dominated by this value. All other zeros contribute to the background scattering phase $\eta_0^{p,b}$.

Now, the single-pole expansion of the S matrix reads as

$$s_{0,11}^{(0)p}(k_1) = s_{0,11}^{p,b}(k_1)s_{0,11}^{p,r}(k_1) = e^{2i\eta_0^{p,b}} \frac{\mathcal{K}_1 - ik_1}{\mathcal{K}_1 + ik_1}, \qquad (47)$$

and the background scattering phase is approximated from a Taylor series at $k_1 = 0$ of Eqs. (45) and (47) up to linear order as

$$\eta_0^{p,b}(k_1) = \frac{1}{2i} \ln \frac{s_{0,11}^{(0)}}{s_{0,11}^{p,r}} \approx n\pi + (1 - a_{\rm sc}\mathcal{K}_1)\frac{k_1}{\mathcal{K}_1}. \qquad (48)$$

The mathematical phase ambiguity is resolved physically by Levinson's theorem, counting the number of bound states $n \in \mathbb{N}_0$ [33]. Moreover, we denote the s-wave scattering length for the square-well potential [28] as $a_{\rm sc} = 1 - \tan \kappa_1/\kappa_1$. The
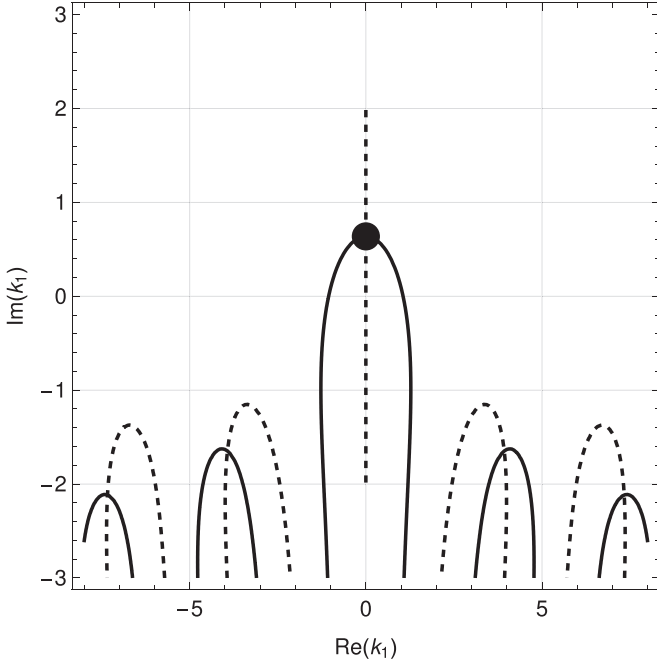
FIG. 3. Zero contour lines of the s-wave Jost function $\Re \mathscr{f}_{0,11}^{(0)}(k_1) = 0$ (solid line) and $\Im \mathscr{f}_{0,11}^{(0)}(k_1) = 0$ (dashed line) in the complex k_1 plane for a potential depth $\kappa_1^2 = 4$. The black dot indicates the position of a bound state at $k_1 = i\mathscr{K}_1 = 0.638i$ and corresponds to a binding energy of $E_r = -\mathscr{K}_1^2 = -0.407$.

resonance contribution $\eta_0^{p,r}$ can be obtained from the second term in Eq. (47). For real k_1, it can be transformed into

$$\eta_0^{p,r}(k_1) = -\arctan\frac{k_1}{\mathscr{K}_1}, \tag{49}$$

using trigonometric relations [34]. Consequently, the single-pole expansion of the total scattering phase (21) is

$$\eta_0^p(k_1) = n\pi + (1 - a_{\mathrm{sc}}\mathscr{K}_1)\frac{k_1}{\mathscr{K}_1} - \arctan\frac{k_1}{\mathscr{K}_1}. \tag{50}$$

In Fig. 4, the scattering phase η_0^p of the pole expansion is compared to the exact scattering phase η_0. It can be seen that
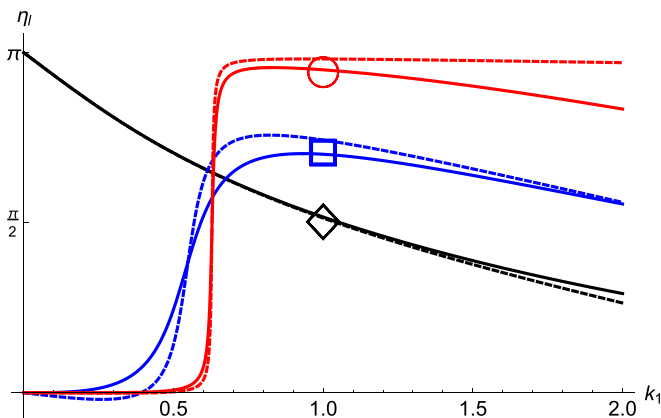

FIG. 4. Exact scattering phase $\eta_l(k_1)$ (solid line) and single-pole approximation $\eta_l^p(k_1)$ (dashed line) versus k_1 for the $l = 0$ (black, $\diamond$), $l = 1$ (blue, $\square$), and $l = 2$ (red, $\circ$) partial waves.
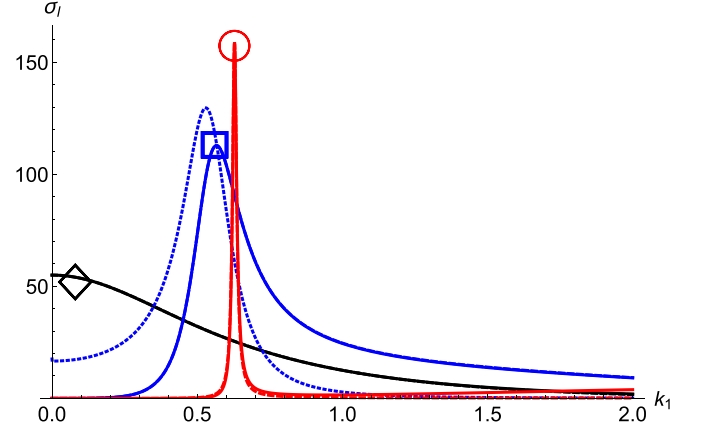

FIG. 5. The exact partial cross section $\sigma_{l,11}^{(0)}(k_1)$ (solid line) and the single-pole approximation (dashed line) versus k_1 for $l = 0$ (black, $\diamond$), $l = 1$ (blue, $\square$), and $l = 2$ (red, $\circ$) partial waves are almost indistinguishable. Using only the Breit-Wigner approximation $\sigma_{l=1,11}^{(0)p,r}(k_1)$ (dotted, blue line) of Eq. (58) leads to significant deviations in shape and resonance position $k_r = \sqrt{E_r} = 0.530$ (vertical black line).

they coincide almost perfectly for small wave numbers. We have chosen the potential depth parameter to accommodate one bound state, thus, the scattering phase approaches π at threshold. Analogously, we depict in Fig. 5 the exact s-wave elastic cross sections of Eq. (23) with the pole expansion. On the scale shown in the figure, there is hardly any difference.

B. Scattering in the p channel

In contrast to the s channel, one can not have any virtual states for higher angular momenta. Resonant states with energies below the angular momentum barrier are called quasibound states.

1. Exact solution

For $l = 1$, the Jost function of Eq. (35) becomes

$$\mathscr{f}_{1,11}^{(0)}(k_1) = \frac{e^{ik_1}\sin q_1}{q_1^3}\left(k_1^2 q_1 \cot q_1 + \kappa_1^2 - ik_1 q_1^2\right), \tag{51}$$

and the uncoupled S-matrix element can be derived from Eq. (20) as

$$s_{1,11}^{(0)}(k_1) = e^{-2ik_1}\frac{k_1^2 q_1 \cot q_1 + \kappa_1^2 + ik_1 q_1^2}{k_1^2 q_1 \cot q_1 + \kappa_1^2 - ik_1 q_1^2}. \tag{52}$$

The corresponding scattering phase is given by

$$\eta_1(k_1) = n\pi - k_1 + \arctan\frac{k_1 q_1^2}{k_1^2 q_1 \cot q_1 + \kappa_1^2}. \tag{53}$$

Again, the physical scattering phase is determined by the number of bound states n in the p-wave potential.

2. Two-pole expansion

The p-wave potential with well depth κ_1^2 given in Table I, supports one quasibound state. Mathematically, it is represented by two closely spaced zeros $k_1 = \{\mathscr{k}_1, -\mathscr{k}_1^*\}$ of the p-wave Jost function in the complex k_1 plane. Its zero contours
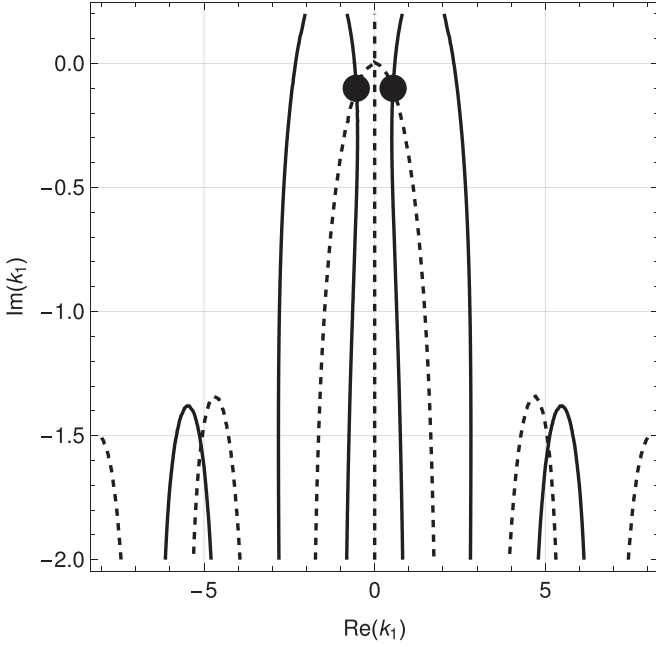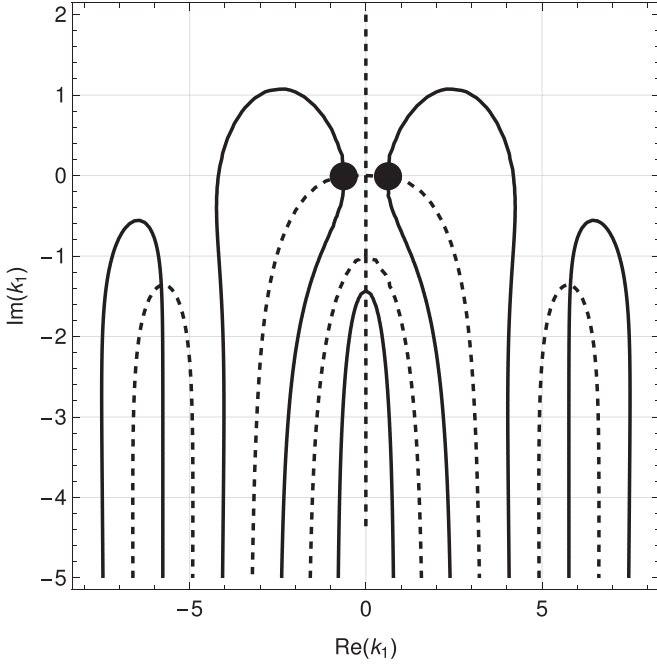
FIG. 6. Zero contour lines of the p-wave Jost function $\Re f_{1,11}^{(0)}(k_1) = 0$ (solid line) and $\Im f_{1,11}^{(0)}(k_1) = 0$ (dashed line) in the complex k_1 plane for a potential depth $\kappa_1^2 = 9$. The black dots indicate the positions $\mathscr{k}_1 = 0.539 - 0.100i$ and $-\mathscr{k}_1^*$.

are shown in Fig. 6. For low values of the wave number, the Weierstrass expansion of the Jost function is dominated by the pair of zeros. All the other zeros contribute cumulatively to the background scattering phase $\eta_1^{p,b}$. Then, the two-pole expansion of the S matrix reads as

$$s_{1,11}^{(0)p}(k_1) = s_{1,11}^{p,b} \, s_{1,11}^{p,r} = e^{2i\eta_1^{p,b}} \frac{(\mathscr{k}_1 + k_1)(\mathscr{k}_1^* - k_1)}{(\mathscr{k}_1^* + k_1)(\mathscr{k}_1 - k_1)}, \quad (54)$$

and $\eta_1^{p,b}$ is found from Eqs. (52) and (54)

$$\eta_1^{p,b}(k_1) = \frac{1}{2i} \ln \frac{s_{1,11}^{(0)}}{s_{1,11}^{p,r}} \approx n\pi + \frac{2k_1 \Im \mathscr{k}_1}{|\mathscr{k}_1|^2}, \quad (55)$$

with a Taylor series at threshold $k_1 = 0$ up to linear order. The resonance scattering phase is defined by the second term in Eq. (54) and one finds, for real k_1,

$$\eta_1^{p,r}(k_1) = -\arctan \frac{2k_1 \Im \mathscr{k}_1}{|\mathscr{k}_1|^2 - k_1^2}. \quad (56)$$

Then, the total scattering phase of the pole expansion reads as

$$\eta_1^p(k_1) = n\pi + \frac{2k_1 \Im \mathscr{k}_1}{|\mathscr{k}_1|^2} - \arctan \frac{2k_1 \Im \mathscr{k}_1}{|\mathscr{k}_1|^2 - k_1^2}. \quad (57)$$

In Fig. 4, the scattering phase η_1^p of the pole expansion is compared to the exact solution η_1. The phase vanishes at zero energy as there is no bound state. While there is good qualitative overall agreement, there are noticeable deviations around the resonance position.

The resonant part of the elastic cross section can be evaluated by inserting $s_{1,11}^{p,r}$ in Eq. (23) and one obtains the

Breit-Wigner formula [32]

$$\sigma_{1,11}^{(0)p,r}(k_1) = \frac{12\pi}{\Re^2 \mathscr{k}_1} \frac{(\Gamma_1/2)^2}{(k_1^2 - \varkappa_1^2)^2 + (\Gamma_1/2)^2}, \quad (58)$$

$$\Gamma_l = 4\Re \mathscr{k}_l \Im \mathscr{k}_l, \quad (59)$$

$$E_r = \varkappa_l^2 = \Re^2 \mathscr{k}_l - \Im^2 \mathscr{k}_l, \quad (60)$$

where we have introduced a resonance energy E_r and a width Γ_l. In Fig. 5, we compare the p-wave elastic cross sections (23) from the exact S matrix $s_{1,11}^{(0)}$ with the pole expansion $s_{1,11}^{(0)p}$ and find excellent agreement. Using only the Breit-Wigner approximation, Eq. (58) leads to significant deviations.

C. Scattering in the d channel

D-wave scattering is qualitatively similar to the p-wave results. However, the increasing complexity of the exact solution conceals the physics. Only the pole expansion unveils the essential resonance features.

1. Exact solution

For $l = 2$, the Jost function of Eq. (35) reads as

$$f_{2,11}^{(0)}(k_1) = \frac{e^{ik_1} \sin q_1}{q_1^5} \big[(k_1^4 - 3\kappa_1^2 + 3ik_1\kappa_1^2 + k_1^2\kappa_1^2)$$

$$\times q_1 \cot q_1 - i(k_1^5 + 3i\kappa_1^2 + 3k_1\kappa_1^2 + k_1^3\kappa_1^2) \big]. \quad (61)$$

The S-matrix element follows from Eq. (20) as

$$s_{2,11}^{(0)}(k_1) = \frac{f_{2,11}^{(0)}(-k_1)}{f_{2,11}^{(0)}(k_1)}, \quad (62)$$

and for real k_1 the scattering phase reads as

$$\eta_2(k_1) = n\pi - k_1$$

$$- \arctan \frac{k_1\big[(k_1^4 + 3\kappa_1^2 + k_1^2\kappa_1^2) - 3\kappa_1^2 q_1 \cot q_1\big]}{(k_1^4 - 3\kappa_1^2 + k_1^2\kappa_1^2)q_1 \cot q_1 + 3\kappa_1^2}. \quad (63)$$

2. Two-pole expansion

The quasibound state of the d-wave potential emerges from two zeros $k_1 = \{\mathscr{k}_2, -\mathscr{k}_2^*\}$ of the Jost function $f_{2,11}^{(0)}(k_1)$ in the complex k_1 plane. Its zero contours are shown in Fig. 7. We assume that the pole expansion of the S matrix

$$s_{2,11}^{(0)p}(k_1) = s_{2,11}^{p,b}(k_1)s_{2,11}^{p,r}(k_1)$$

$$= e^{2i\eta_2^{p,\mathrm{bg}}(k_1)} \frac{(\mathscr{k}_2 + k_1)(\mathscr{k}_2^* - k_1)}{(\mathscr{k}_2^* + k_1)(\mathscr{k}_2 - k_1)} \quad (64)$$

is dominated by the two poles for low k_1. The effect of all the other poles contributes to the background scattering phase $\eta_2^{p,b}$. Using Eqs. (62) and (64), the background scattering phase is found from a Taylor series at $k_1 = 0$ up to linear order as

$$\eta_2^{p,b}(k_1) = \frac{1}{2i} \ln \frac{s_{2,11}^{(0)}}{s_{2,11}^{p,r}} \approx n\pi + \frac{2k_1 \Im \mathscr{k}_2}{|\mathscr{k}_2|^2}. \quad (65)$$

FIG. 7. Zero contour lines of the d-wave Jost function $\Re f^{(0)}_{2,11}(k_1) = 0$ (solid line) and $\Im f^{(0)}_{2,11}(k_1) = 0$ (dashed line) in the complex k_1 plane for a potential depth $\kappa^2_2 = 19.5$. The black dots indicate the positions $\mathscr{k}_2 = 0.628 - 0.009i$ and $-\mathscr{k}^*_2$.

It has the same structure as the p-wave result (55), which presumably holds also for higher angular momenta. It holds definitely for the resonance phase as the structure of the Weierstrass expansion is identical. Therefore, the total scattering phase for the pole expansion reads as

$$\eta^p_2(k_1) = n\pi + \frac{2k_1\Im\mathscr{k}_2}{|\mathscr{k}_2|^2} - \arctan\frac{2k_1\Im\mathscr{k}_2}{|\mathscr{k}_2|^2 - k^2_1}, \quad (66)$$

analogously to Eq. (57).

In Fig. 4, the scattering phase η^p_2 of the pole expansion is compared to the exact solution η_2. Around the resonance position and for larger k_1, η^p_2 deviates from the exact solution. In Fig. 5, the d-wave elastic cross sections (23) found from the exact S matrix $s^{(0)}_{2,11}$ and found from the pole expansion $s^{(0)p}_{2,11}$ are compared. Only for larger k_1 the solutions start to deviate from each other, the resonant behavior is explained perfectly by the pole expansion.

V. TWO-BODY LOSS RATES

Now, we will extend the discussion from the single-channel case to the coupled two-channel case within the DWBA. We use the same potential parameters for the upper channel as in the single-channel case given in Table I. The weakly bound s state in the upper channel as well as the quasibound p and d states will dominate the behavior of the partial two-body loss rates as the channels are only weakly coupled to the loss channels. Given a sufficiently large separation of channel threshold energies $\Delta_{11} \gg \Delta_{22}$, one can assume that the potential depth κ^2_2 of channel 2 does not influence the scattering behavior of channel 1. For simplicity, we have chosen them equal. All other parameters are listed in Table II.

TABLE II. Potential parameters of two-channel scattering used in the examples.

Angular momentum	l	0	1	2
Potential depth	κ^2_2	4.0	9.0	19.5
Threshold energy channel 1	Δ_{11}	0.0	0.0	0.0
Threshold energy channel 2	Δ_{22}	−3.0	−3.0	−3.0
Coupling strength	v_{12}	0.1	0.1	0.1

The transition amplitude between the channels is determined by the S-matrix element $s^{(1)}_{l,12}$ of Eq. (37). Its poles follow from the zeros of the uncoupled Jost functions $f^{(0)}_{l,11}$, $f^{(0)}_{l,22}$ of channels 1 and 2, respectively.

We present the zero contours of the s-wave Jost functions $f^{(0)}_{l,11}$ and $f^{(0)}_{l,22}$ in Fig. 8, and in Fig. 9 the p-wave result. It can be seen that the zeros of $f^{(0)}_{l,22}$ are further away from the origin than the smallest zero(s) of $f^{(0)}_{l,11}$ marked in blue. A similar picture arises for $l = 2$. Therefore, we assume that the pole expansion of $s^{(1)}_{l,12}$ is dominated by the zeros of $f^{(0)}_{l,11}$ at $k_1 = i\mathscr{K}_1$ ($l = 0$) and the pair of zeros $k_1 = \{\mathscr{k}_l, -\mathscr{k}^*_l\}$ for $l = 1, 2$. Nonresonant features contribute to the background scattering phase $\eta^{p,b}_{l,12}$. We obtain for the pole expansion

$$s^{(1)p}_{0,12}(k_1) = \frac{a_0 k^{\frac{1}{2}}_1 e^{\xi^{p,b}_{0,12}(k_1)}}{\mathscr{K}_1 + ik_1}, \quad (67)$$

$$s^{(1)p}_{l,12}(k_1) = \frac{a_l k^{\frac{2l+1}{2}}_1 e^{\xi^{p,b}_{l,12}(k_1)}}{(\mathscr{k}^*_l + k_1)(\mathscr{k}_l - k_1)}, \quad (68)$$
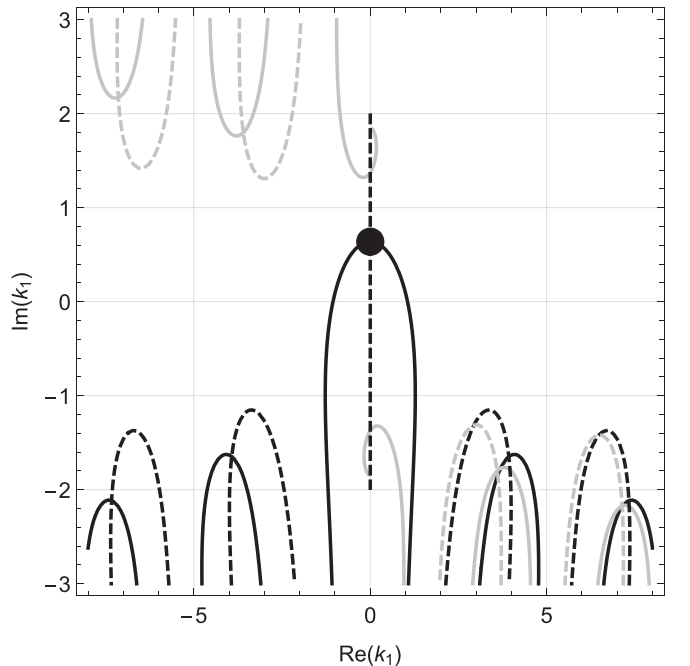

FIG. 8. Zero contour lines of the s-wave Jost functions in channels 1 and 2: $\Re f^{(0)}_{0,11}(k_1) = 0$ (solid, black line), $\Im f^{(0)}_{0,11}(k_1) = 0$ (dashed, black line), and $\Re f^{(0)}_{0,22}(k_1) = 0$ (solid, gray line), $\Im f^{(0)}_{0,22}(k_1) = 0$ (dashed, gray line) in the complex k_1 plane. The black dot indicates the position $k_1 = i\mathscr{K}_1 = 0.638i$. The potential parameters are given in Table II.
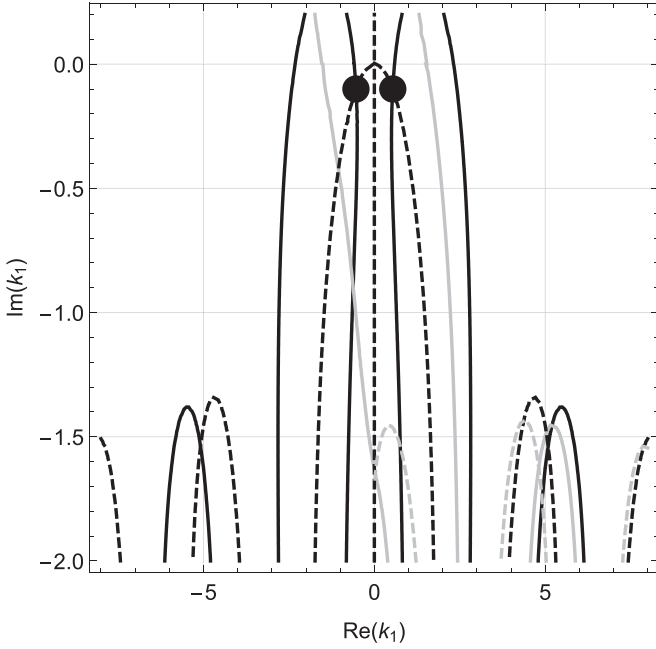
FIG. 9. Zero contour lines of p-wave Jost function in channels 1 and 2: $\Re f_{1,11}^{(0)} = 0$ (solid, black line), $\Im f_{1,11}^{(0)} = 0$ (dashed, black line), and $\Re f_{1,22}^{(0)} = 0$ (solid, gray line), $\Im f_{1,22}^{(0)} = 0$ (dashed, gray line) in the complex k_1 plane. The black dots indicate the positions $\mathcal{k}_1 = 0.539 - 0.100i$ and $-\mathcal{k}_1^*$. The potential parameters are given in Table II.

where the second line holds for $l > 0$ and the background attenuation coefficients are given by

$$\xi_{0,12}^{p,b}(k_1) = \ln\left[s_{0,12}^{(1)}(k_1) \frac{(\mathscr{K}_1 + ik_1)}{a_0\sqrt{k_1}} \right]$$
$$= \frac{1}{2}\left(b_0 k_1 + c_0 k_1^2 + \cdots\right), \tag{69}$$

$$\xi_{l,12}^{p,b}(k_1) = \ln\left[s_{l,12}^{(1)}(k_1) \frac{(\mathcal{k}_l^* + k_1)(\mathcal{k}_l - k_1)}{a_l k_1^{\frac{2l+1}{2}}} \right]$$
$$= \frac{1}{2}\left(b_l k_1 + c_l k_1^2 + \cdots\right). \tag{70}$$

Here, a Taylor expansion of the background scattering phases around $k_1 = 0$ yields expansion coefficients $a_l, b_l, c_l, \ldots$, which depend on the potential parameters and the pole positions.

From this expansion, one can obtain the two-body loss rates of Eq. (26). In lowest order, they read as

$$\beta_0^{(1)p}(k_1) = \frac{2\pi |a_0|^2}{k_1^2 + \mathscr{K}_1^2}, \tag{71a}$$

$$\beta_l^{(1)p}(k_1) = \frac{2\pi(2l+1)|a_l|^2}{\left(k_1^2 - \varkappa_l^2\right)^2 + (\Gamma_l/2)^2} k_1^{2l}. \tag{71b}$$

An important feature of the pole expansion of the two-body loss rates in Eqs. (71) is the power-law behavior k_1^{2l}. This is known as the *Wigner threshold behavior* [35–37].

In Fig. 10, we compare the partial two-body loss rates of the DWBA (26) with the pole expansion (71). The pole expansion
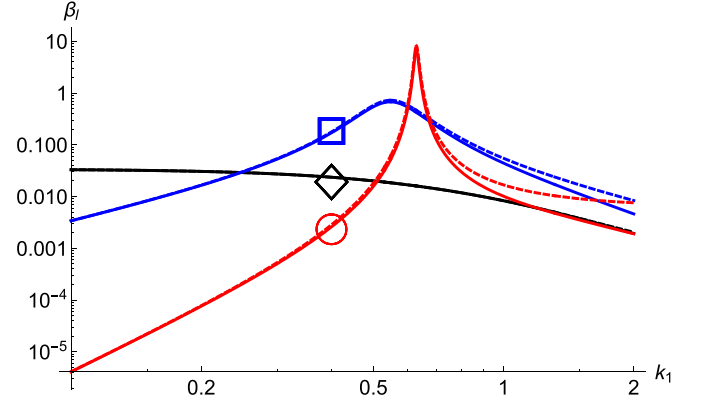

FIG. 10. DWBA partial-wave two-body loss rates $\beta_l^{(1)}$ (solid line) and the single-pole approximation $\beta_l^{(1)p}$ (dashed line) versus channel wave number k_1 for $l = 0$ (black, ◇), $l = 1$ (blue, □), $l = 2$ (red, ○) for the potential parameters of Table II.

describes the low-energy and the resonant behavior of the two-body loss rates very well and starts to deviate from the DWBA solution only beyond the resonance positions.

VI. ANALYSIS OF SYNTHETIC SCATTERING DATA WITH SHAPE FUNCTIONS

Here, we employ the pole expansion of the partial two-body loss rates (71) to analyze the synthetic scattering data of [27] for heteronuclear ^{20}Ne and ^{21}Ne PI and AI collisions. In the simulations of [27], the two-body loss rate β was calculated in terms of a partial-wave decomposition

$$\beta = \frac{1}{2}\sum_l \beta_l, \tag{72}$$

with the partial two-body loss rates β_l. The factor $\frac{1}{2}$ accounts for the collisions of nonidentical particles [38]. In the experimental temperature regime $T \simeq 1$ mK, only few partial waves $l \leqslant 2$ contribute to the total loss rate.
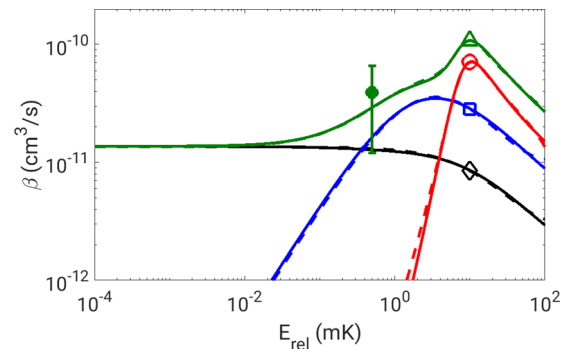

FIG. 11. Synthetic scattering two-body loss rates β^{synt} (solid, green, △) and pole expansion β^p (dashed, green, △) with the coefficients of Table III versus relative collisions energy $E_{\text{rel}} = \hbar k^2/2\mu$ in units of k_B for ^{21}Ne and ^{20}Ne collisions. Additionally shown are the partial-wave contributions $1/2 \times \beta_l^{\text{synt}}$ [solid, (black, ◇), (blue, □), (red, ○)], $1/2 \times \beta_l^p$ [dashed, (black, ◇), (blue, □), (red, ○)] for $l = 0, 1, 2$, respectively, and experimental data point (green filled circle with error bars).

TABLE III. Expansion coefficients and pole positions found from fit of β_l^p to the synthetic data.

	$l = 0$	$l = 1$	$l = 2$
a_l	0.1477	0.1326	2.3141
Re c_l	57.3641	76.8736	−64.7843
Re e_l			−642.3825
$\mathscr{K}_l$	0.0408		
Re $\mathscr{k}_l$		$1.5e^{-10}$	0.0304
Im $\mathscr{k}_l$		−0.0198	−0.0100

In order to obtain a high-quality interpolation of the two-body loss rates of the available synthetic scattering data, we have to consider the higher-order corrections of Eqs. (69) and (70) in the two-body loss rates of Eq. (26) and find

$$\beta_0^p(k) = \frac{2\pi |a_0|^2}{k^2 + \mathscr{K}_1^2} e^{\Re c_0 k^2}, \tag{73a}$$

$$\beta_1^p(k) = \frac{6\pi |a_1|^2}{\left(k^2 - \varkappa_1^2\right)^2 + (\Gamma_1/2)^2} k^2 e^{\Re c_1 k^2}, \tag{73b}$$

$$\beta_2^p(k) = \frac{10\pi |a_2|^2}{\left(k^2 - \varkappa_2^2\right)^2 + (\Gamma_2/2)^2} k^4 e^{\Re(c_2 k^2 + e_2 k^4)}. \tag{73c}$$

In the additional attenuation factors of the two-body loss rates, all odd power of k_1 vanish as the coefficients $b_l, d_l, \ldots$ are purely imaginary.

A least-square fit of the partial two-body loss rates in Eqs. (73a), (73b), and (73c) to the synthetic data of Ref. [27] leads to the coefficients given in Table III.

In Fig. 11, we compare the synthetic data with the optimal fits from the shape functions obtained from the pole expansion. We also included the single available experimental data point from Ref. [11] to the picture. It can be seen that the pole expansion agrees very well with the synthetic data as well as with the experimental data point. Technically speaking, the two-body loss rates should be averaged thermally to match the experimental data point. However, the width of the relative velocity distribution in the thermal gas is large compared to the widths of the two-body loss rates. Moreover, the error bar for the experimental data point is large, too. Therefore, we neglect the effects of thermal averaging.

VII. CONCLUSION

In this article, we have presented a coupled two-channel model for the reactive collisions of atoms at low collision energies. Transition from the elastic scattering channel to the lower ionization channel models loss of atoms in two-body collisions. Examples for these two-body losses are autoionization and Penning ionization processes. In particular, we study the two-channel square-well model. On one hand, this model can be solved in closed form and, on the other hand, one can use the pole approximation to obtain physically motivated shape functions from it. To extract useful approximations, we employed the distorted-wave Born approximation and studied the poles in the complex k_1 plane for the lowest s, p, and d partial waves. From this analysis, we obtain simple analytic

expressions for the partial two-body loss rates. Fitting these analytic two-body loss rates to available synthetic scattering data [27] on cold heteronuclear ^{20}Ne and ^{21}Ne collisions gives very good agreement and also matches the experimental data point of Ref. [11].

APPENDIX A: RICCATI-BESSEL FUNCTIONS

Bessel functions are a core element of three-dimensional scattering theory. In order to avoid definitional ambiguities, we use the Riccati-Hankel functions

$$\hat{h}_l^\pm(z) \equiv \hat{n}_l(z) \pm i \, \hat{j}_l(z), \tag{A1}$$

as in Ref. [29], where $\hat{j}_l(z)$ is the Riccati-Bessel function and $\hat{n}_l(z)$ is the Riccati-Neumann function [39]

$$\hat{j}_l(z) \equiv \sqrt{\frac{\pi z}{2}} J_{l+\frac{1}{2}}(z), \tag{A2}$$

$$\hat{n}_l(z) \equiv (-1)^l \sqrt{\frac{\pi z}{2}} J_{-l-\frac{1}{2}}(z), \tag{A3}$$

with the Bessel function of the first kind $J_l(z)$. The Riccati-Hankel functions have the symmetry properties

$$\hat{h}_l^\pm(-z) = (-1)^{l+1} \hat{h}_l^\mp(z). \tag{A4}$$

The behavior of $\hat{j}_l(z)$ for small arguments z is given by

$$\hat{j}_l(z) \xrightarrow[z \to 0]{} \frac{z^{l+1}}{(2l+1)!!}. \tag{A5}$$

APPENDIX B: ANALYTIC POLE APPROXIMATION

One can determine the zeros of the Jost function $\mathscr{f}_{l,11}^{(0)}$ in the complex k_1 plane either numerically or analytically by introducing simple approximations. In the case of the s-wave Jost function (44), one can use complex transformations $k_1 \equiv z\kappa_1$, $z \equiv -i \cos w$ to find

$$\kappa_1 \sin w = w + n\pi, \quad n \in \mathbb{N}_0^+. \tag{B1}$$

By solving this equation for w and for all n, we obtain all zeros of $\mathscr{f}_{0,11}^{(0)}$. For the zeros close to the origin of the complex plane, we can assume $|k_1|/\kappa_1 \ll 1$ and it follows $w \simeq \pi/2$. A Taylor series of (B1) at $w = \pi/2$ to second order leads to

$$w_\pm = \frac{-1 + \pi\kappa_1 \pm \sqrt{1 - \pi\kappa_1 - 2n\pi\kappa_1 + 2\kappa_1^2}}{\kappa_1}. \tag{B2}$$

The zero of the Jost function due to the first bound state of the potential is given by w_+ and $n = 0$, the zero of the Jost

function due to the second bound state by w_+ and $n = 1$, and so forth. For N bound states present in the scattering potential, the zero of the Jost function of the first virtual state is given by w_+ for $n = N$, for the second virtual state by w_+ for $n = N + 1$, and so forth up to $n = N + N' - 1$ for N' virtual states present. The zeros of the Jost function due to scattering

resonances are given by the two solutions $w_\pm$ for $n > N + N' - 1$.

For $\kappa_1 = 4$ and $n = 0$, we find $w_+ = 1.895$ from Eq. (B2). Resubstitution leads to a zero of the Jost function at $\hbar_1 = i\mathscr{K}_1$ with $\mathscr{K}_1 = 0.637$. The numerically determined value is given by $\mathscr{K}_1 = 0.638$.

[1] F. Penning, Naturwissenschaften **15**, 818 (1927).

[2] P. E. Siska, Rev. Mod. Phys. **65**, 337 (1993).

[3] W. Vassen, C. Cohen-Tannoudji, M. Leduc, D. Boiron, C. I. Westbrook, A. Truscott, K. Baldwin, G. Birkl, P. Cancio, and M. Trippenbach, Rev. Mod. Phys. **84**, 175 (2012).

[4] H. Friedrich, *Scattering Theory* (Springer, Berlin, 2013).

[5] R. J. W. Stas, J. M. McNamara, W. Hogervorst, and W. Vassen, Phys. Rev. A **73**, 032713 (2006).

[6] J. M. McNamara, R. J. W. Stas, W. Hogervorst, and W. Vassen, Phys. Rev. A **75**, 062715 (2007).

[7] A. S. Dickinson, J. Phys. B: At., Mol. Opt. Phys. **40**, F237 (2007).

[8] C. Orzel, M. Walhout, U. Sterr, P. S. Julienne, and S. L. Rolston, Phys. Rev. A **59**, 1926 (1999).

[9] H. Katori, H. Kunugita, and T. Ido, Phys. Rev. A **52**, R4324 (1995).

[10] P. Spoden, M. Zinner, N. Herschbach, W. J. van Drunen, W. Ertmer, and G. Birkl, Phys. Rev. Lett. **94**, 223201 (2005).

[11] J. Schütz, T. Feldker, H. John, and G. Birkl, Phys. Rev. A **86**, 022713 (2012).

[12] J. Schütz, A. Martin, C. Cop, R. Walser, and G. Birkl (unpublished).

[13] M. Berglund and M. Wieser, Pure Appl. Chem. **83**, 397 (2011).

[14] S. Kotochigova, E. Tiesinga, and I. Tupitsyn, Phys. Rev. A **61**, 042712 (2000).

[15] S. Kotochigova (private communication).

[16] A. Derevianko and A. Dalgarno, Phys. Rev. A **62**, 062501 (2000).

[17] Z. Idziaszek and P. S. Julienne, Phys. Rev. Lett. **104**, 113202 (2010).

[18] K. Jachymski, M. Krych, P. S. Julienne, and Z. Idziaszek, Phys. Rev. Lett. **110**, 213202 (2013).

[19] K. Jachymski, M. Krych, P. S. Julienne, and Z. Idziaszek, Phys. Rev. A **90**, 042705 (2014).

[20] Z. Idziaszek, A. Simoni, T. Calarco, and P. S. Julienne, New J. Phys. **13**, 083005 (2011).

[21] P. S. Julienne, Faraday Discuss. **142**, 361 (2009).

[22] G. Quemener and J. L. Bohn, Phys. Rev. A **81**, 022702 (2010).

[23] Z. Idziaszek, G. Quéméner, J. L. Bohn, and P. S. Julienne, Phys. Rev. A **82**, 020703 (2010).

[24] S. Kotochigova, New J. Phys. **12**, 073041 (2010).

[25] P. S. Julienne, T. M. Hanna, and Z. Idziaszek, Phys. Chem. Chem. Phys. **13**, 19114 (2011).

[26] M. D. Frye, P. S. Julienne, and J. M. Hutson, New J. Phys. **17**, 045019 (2015).

[27] C. Cop, A. Martin, G. Birkl, and R. Walser (unpublished).

[28] J. T. M. Walraven, *Lecture Notes: Quantum Gases* (Les Houches, 2017), https://staff.fnwi.uva.nl/j.t.m.walraven/walraven/Lectures.htm.

[29] J. Taylor, *Scattering Theory: The Quantum Theory of Nonrelativistic Collisions* (Dover, New York, 2006).

[30] E. Freitag and R. Busam, *Complex Analysis*, 2nd ed. (Springer, Berlin, 2009).

[31] J. B. Conway, *Functions of One Complex Variable: 1*, 2nd ed., Graduate Texts in Mathematics (Springer, New York, 2010), Vol. 11.

[32] R. Newton, *Scattering Theory of Waves and Particles*, 2nd ed. (Dover, New York, 2002).

[33] For simplicity, we want to consider an integer number of bound states and do not want to discuss the well-known limit of half-bound states.

[34] For a real angle α, following useful identity has been employed repeatedly: $\arctan \alpha = \frac{1}{2i} \ln \frac{1+i\alpha}{1-i\alpha} + n\pi$.

[35] P. S. Julienne and F. H. Mies, J. Opt. Soc. Am. B **6**, 2257 (1989).

[36] H. A. Bethe, Phys. Rev. **47**, 747 (1935).

[37] E. P. Wigner, Phys. Rev. **73**, 1002 (1948).

[38] J. Weiner, V. S. Bagnato, S. Zilio, and P. S. Julienne, Rev. Mod. Phys. **71**, 1 (1999).

[39] M. Abramowitz and I. Stegun, *Handbook of Mathematical Functions* (Dover, New York, 1965).